Robust Control of Autonomous Remotely Operated Vehicles at Exposed Aquaculture Sites.

Kenny Hoang Nguyen, Walter Caharija, Sveinung Johan Ohrem, Jan Tommy Gravdahl, Antonio Loria, Herman Biørn Amundsen

Robust Control of Autonomous Remotely Operated Vehicles at Exposed Aquaculture Sites

Kenny Hoang Nguyen, Walter Caharija, Sveinung Johan Ohrem,
Jan Tommy Gravdahl, Antonio Loria, Herman Biørn Amundsen

***Abstract*— This paper presents two adaptive nonlinear controllers for robust velocity and heading control of a remotely operated vehicle navigating in exposed aquaculture sites. The controllers are designed to make it possible for the vehicle to execute autonomous traversal of an aquaculture net pen using a net-following guidance algorithm, in the presence of significant environmental disturbances. Each of these controllers is tailored for different physical models depending on the application scenario. The first is suitable for slow-speed maneuvers and the second applies to cases in which aggressive maneuvers are needed. The second model has the added difficulty that additional Coriolis-forces nonlinearities must be considered. Stability proofs for the closed-loop system under the action of each controller are provided. For the first controller, the closed-loop system is proven to be uniformly globally asymptotically stable and uniformly locally exponentially stable at the origin. For the second controller the origin of the closed-loop system is proven to be uniformly globally stable and asymptotic convergence of the velocity and heading error states are provided for the second control law. In addition, the paper presents simulation and experimental results to validate and illustrate the theoretical analysis, where the controllers are applied to an industrial underwater robot. In particular, the first control law was successfully tested at a full-scale aquaculture site under realistic operational conditions.**

Index terms—adaptive control, non-linear control, modelling, remotely operated vehicle (ROV), aquaculture, path following.

I. Introduction

A. Motivation

Salmon farming is expanding at a steady pace worldwide to meet the growing demand for food [1]. The Norwegian aquaculture industry contributed in 2021 to approximately half of the world production of farmed salmon, accounting for 1.6 million metric tonnes with an export value of 6.9 bn. EUR [2]. In order to increase production and mitigate some of the issues related to today's farming methods, such as sea lice infestations, several operators in the industry are moving the production to more exposed areas, a trend supported by Norwegian authorities [3]. The Norwegian Ministry of Trade, Industry and Fisheries regulates the growth of the aquaculture industry to reduce the environmental impact caused by e.g., increased sea lice infestations, escape of farmed fish, and the welfare of farmed fish in production areas [4].

Remotely Operated Vehicles (ROVs) have been introduced in aquaculture as a technology that can assist farmers and operators in meeting the increasing requirements for inspection of aquaculture structures from the governing bodies. To some extent, ROVs replace divers in hazardous operations [5]. ROV operations in aquaculture are challenging since ROV operators are required to manage concurring tasks. In fact, they must navigate and maneuver the vehicle in a dynamic unstructured environment while they simultaneously monitor the fish, inspect the structure or perform operations such as cleaning of nets and mooring lines. Operators execute these demanding tasks assisted only by elementary automatic functions such as automatic heading and depth control.

Therefore, both ROV operators and fish farmers may benefit from more autonomous features when it comes to control of ROVs, as autonomy decreases costs and makes operations more effective [6]. Such autonomous functionalities must feature robustness towards environmental disturbances as the industry is moving towards more exposed locations where the effects of ocean currents and waves are stronger, compared to today's locations closer to the shore. Robust control laws are therefore required to maintain a specific heading angle, track a velocity profile, or follow a path. In particular, this paper proposes two non-linear adaptive controllers for robust velocity and heading control of fully actuated ROVs operating at exposed aquaculture sites.

B. Previous Work

Velocity and heading controllers for vehicles such as ROVs are often based on the linear proportional-derivative (PD), proportional-integral (PI) or proportional-integral-derivative (PID) architectures. These controllers may be sufficient in ideal scenarios [7], but their performance may be unsatisfactory in the presence of large spatial and temporal variations in the environment, and in the presence of nonlinearities. Continuous re-adjustment of controller gains may be necessary to obviate large offsets and oscillatory behavior [8].

This work has been funded by the Norwegian Research Council through the Center for Research Based Innovation (SFI) Exposed (grant no. 237790). Other funding sources include the SINTEF RACE internal funding scheme and the Norwegian Research Council project CHANGE (grant no. 313737). The authors greatly appreciate the funding. The authors would also like to extend their gratitude to the personnel at the SINTEF ACE research infrastructure for assisting in field trials.

Kenny Hoang Nguyen, Jan Tommy Gravdahl and Herman Biørn Amundsen are with the Dept. Engineering Cybernetics, Norwegian University of Science and Technology, 7030 Trondheim, Norway (email: kennguy@hotmail.no, jan.tommy.gravdahl@ntnu.no, herman.b.amundsen@ntnu.no)

Walter Caharija is with Siemens Energy AS, 7031, Trondheim (email: walter.caharija@siemens-energy.com)

Sveinung Johan Ohrem and Herman Biørn Amundsen are with the Dept. of Aquaculture Technology, SINTEF Ocean AS, 7010 Trondheim (email: sveinung.ohrem@sintef.no, herman.biorn.amundsen@sintef.no)

Antonio Loria is with Centre National de la Recherche Scientifique, 91190 Gif-sur-Yvette, France (email: antonio.loria@cnrs.fr)

Several advanced control strategies have been proposed by the marine control research community to address this lack of robustness and achieve better performance in vehicle control. For instance, adaptive feedback linearizing-based controllers are designed for unmanned marine vehicles in [8]–[10] to compensate for the unknown ocean currents. The proposed controllers are designed for both fully actuated and underactuated marine vehicles. A simplification of the controllers proposed in [8]–[10] is achieved in [11] at the expense of controlling the vehicle's relative velocity instead of controlling its absolute velocity, and under the assumption of the perturbing current being constant and irrotational. Adaptive control of surface vessels is addressed in [12] where specific criteria to achieve strong stability properties and simultaneously estimate the underlying disturbance are given.

Lyapunov-based and backstepping control are used in [13]–[16] to develop a series of robust adaptive course tracking controllers for underactuated ships. Adaptive backstepping is also employed in [17]–[19] to make a surface vessel track a given course and in [20] for dynamic position (DP) of ROVs.

Neural networks and sliding mode control are combined with adaptive backstepping to achieve path following and navigation control of underactuated ships in the works of [21]–[24] under the assumption of sway motion boundedness. All these works rely on assumptions that the model parameters are known.

Sliding mode control is a design method known for its intrinsic robustness features with respect to disturbances and model uncertainties [25]. Therefore, it is often employed in marine control systems [26], [27]. However, a known drawback with some sliding mode controllers compared to other nonlinear controllers is chattering, which increases wear and tear on the actuators. A way to deal with chattering is to use higher-order sliding mode techniques such as the super-twisting algorithm (STA) [28] or variations thereof, including generalized STA and adaptive generalized STA techniques. In [29], both generalized and adaptive generalized STA was used to control an ROV operating at an aquaculture site.

C. Contribution

This paper proposes two nonlinear adaptive controllers for robust velocity and heading control of a fully actuated ROV in three degrees of freedom (DOFs), i.e., surge, sway and yaw, operating in exposed aquaculture sites. Preliminary results can be found in [30]. The two controllers are inspired by the work of [8], [9], [11] where environmental disturbances are modelled as irrotational ocean currents. In contrast to these references, however, in this paper we address the case when it is impossible to control relative velocity and it is simultaneously required to provide an estimation of the prevailing disturbance. The latter requirement is not possible with the higher-order sliding mode techniques of [29], as these offer controller parameter adaptation only.

The papers [8] and [9] demonstrate full-state stabilization of fully actuated and underactuated vehicles with an increased complexity due to the presence of absolute and relative velocities in the system dynamics, and do not provide controllers capable of estimating the underlying disturbance. The integral line-of-sight (ILOS) guidance law, first proposed in [9], is analyzed in [11] with full-state stabilization, but employs a relative velocity approach for underactuated surface vessels as well as underactuated underwater vehicles.

The relative velocity approach of [11] models the ocean current disturbance as a bias in the kinematics of the closed-loop system, thereby making it possible to avoid the unknown terms in the system dynamics. In turn, this simplifies the design of the velocity and heading controllers. This results in strong stability properties for the closed-loop system, i.e., uniform global asymptotic stability (UGAS) and uniform local exponentially stability (ULES) at the origin, or equivalently global κ-exponential stability [31], at the expense of controlling the relative velocity of the vehicle instead of the absolute velocity. In some cases, however, it is impossible to control the relative velocity. This may be due to sensor limitations, or due to the nature of the control objective, e.g., following a certain ground speed, as required by the task addressed in [8]. In such cases, the relative velocity approach from [11] cannot be applied, and alternative velocity and heading control strategies are required if the objective is to achieve robustness, strong stability properties, and a reliable estimation of the prevailing environmental disturbance.

The two controllers proposed in this paper perform absolute velocity control (i.e. ground speed control). In particular, the first controller is derived using a simplified 3-DOF non-linear control plant model, while the second controller considers a more complex, non-linear 3-DOF control plant model. The first controller, hereafter referred to as C1, follows the design strategy outlined in [12] and utilizes an adaptation law to ensure that the origin of the closed-loop system is UGAS and ULES without a persistency of excitation requirement often required by adaptive controllers [32]. The controller is also able to estimate the acting disturbance vector. As opposed to the systems analyzed in [12], [15], [33], the disturbance in this paper is modelled as an irrotational ocean current, and not as a pure force vector. This difference in modeling approach is required as the controllers proposed in this paper are designed for path following or trajectory tracking purposes which have a different velocity range compared to station keeping or weather waning solutions [34].

To validate the theoretical results, the controller C1 is demonstrated in simulations, and in experiments using an industrial ROV. In particular, the controller C1 was successfully tested at a full-scale aquaculture site under realistic operational conditions. The results show that C1 successfully compensates the disturbances under significant spatial variations, and that the ROV follows the given reference signals with negligible offsets and limited transients compared to a PID controller.

The second controller, hereafter referred to as C2, builds on the first but it is tailored for a more complex plant model that takes into account more of the non-linearities in the underlying system. Such non-linearities may arise when high rotational rates (e.g., $r \geq 0.05$ rad/s ≈ 3 deg/s) are generated by aggressive maneuvers, e.g., when the ROV reactively avoids obstacles or follows a net that presents tight bends and sharp corners [35]. Hence, the controller C2 is expected to be

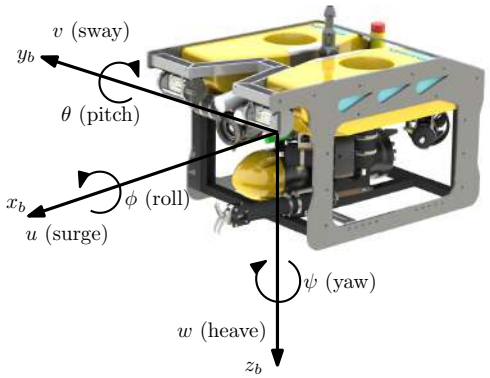

Fig. 1: Body frame axis on the Argus Mini ROV

more robust than C1. In particular, the adaptive law of C2 is expanded to adapt and compensate for unknown higher-order disturbances. For C2, the origin of the closed-loop system is proved to be uniformly globally stable (UGS). Furthermore, it is showed that the velocity and heading error states converge asymptotically and uniformly to zero. The performance of the controller C2 is validated in simulations.

D. Manuscript Structure

The remainder of the paper is structured as follows: Section II introduces the prerequisities for the control plant models, and the control objective. Section III presents the first control law and its stability analysis. Section IV presents the second control law and its stability analysis. Section V presents the simulation setup while Section VI presents the simulations results for both controllers. Section VII presents the results from a full scale trial where controller C1 is compared to a PID controller in similar operating conditions. Lastly, conclusions and proposals for future work are given in Section VIII.

II. Model Prerequisites and Control Objective

A. Model Prerequisites

The control plant models [36] of the ROV are defined based on 3 DOFs: surge, sway and yaw. The kinematics of the vehicle are given in the North-East-Down (NED) frame, denoted $\{n\}$, while the dynamics are described in the body-fixed coordinate frame, denoted $\{b\}$. The local ROV body-fixed frame is illustrated in Figure 1.

For both control plant models the state of the ROV is given by the vector $\begin{bmatrix}\boldsymbol{\eta}^{n^\top} & \boldsymbol{\nu}^{b^\top}\end{bmatrix}^\top$ where $\boldsymbol{\eta}^n = \begin{bmatrix}x & y & \psi\end{bmatrix}^\top$ is the generalized vector describing position and orientation of the ROV in $\{n\}$ and $\boldsymbol{\nu}^b = \begin{bmatrix}u & v & r\end{bmatrix}^\top$ describes the linear and angular velocity of the ROV in $\{b\}$. The following assumptions apply to both presented control plant models:

Assumption 1: The roll and pitch motion of the ROV can be neglected due to passive stabilization properties.

Assumption 2: The ROVs weight and buoyancy are equal (the vehicle is neutrally buoyant), i.e., it will not move in the heave (vertical) direction without influence from an external force. Hence, the motion in heave can be neglected. In addition, the vehicle centre of gravity (CG) and the centre of buoyancy (CB) are located in the same vertical axis in $\{b\}$.

Remark 1: Most ROVs are designed to be slightly positively buoyant so that they rise to the surface, in the case of a system shut down. For all practical purposes the ROV can be assumed to be neutrally buoyant.

Assumption 3: The ROV is symmetric in port-starboard, fore-aft and bottom-top.

Assumption 4: The body-fixed frame center of origin (CO) is located in the CG.

Remark 2: Assumption 1-Assumption 4 are common assumptions when designing control plant models of ROVs and can be found in other works such as [8] and [37].

Assumption 5: The ROV operates at speeds that are less than 2 m/s.

Remark 3: The ROV has four thrusters actuating the DOFs in the horizontal plane. The thrusters have physical limitations and cannot generate enough force for the ROV to achieve speeds over 2 m/s.

Assumption 6: The hydrodynamic damping is linear.

Remark 4: Non-linear damping is not considered in order to reduce the complexity of the controllers. For low-speed maneuvering, Assumption 6 is considered a mild assumption since the passive nature of any non-linear hydrodynamic damping enhances the directional stability of the vehicle, [8], [10]. On the other hand, the linear damping terms dominate the non-linear terms at low speeds.

Assumption 7: The ocean current is constant, irrotational and bounded with a velocity vector $\mathbf{V}_c^n = [V_x\ V_y\ 0]^\top$ in $\{n\}$. Therefore there exists a constant $V_{\max} > 0$ such that $V_{\max} \geq \sqrt{V_x^2 + V_y^2}$. Furthermore, due to the current being constant in the inertial frame $\{n\}$, the time-derivative is $\dot{\mathbf{V}}_c^n = \mathbf{0}$.

B. Control Objective

The primary control objective is to make the vehicle track the desired time-varying velocity and heading references in 3-DOF, in the presence of unknown, constant, and irrotational ocean currents. A secondary objective is to estimate the underlying disturbance, i.e., the ocean current vector. The primary control objective is formalized as follows:

$$\lim_{t\to\infty} |u(t) - u_d(t)| = 0, \tag{1a}$$

$$\lim_{t\to\infty} |v(t) - v_d(t)| = 0, \tag{1b}$$

$$\lim_{t\to\infty} |\psi(t) - \psi_d(t)| = 0, \tag{1c}$$

where $u_d(t)$, $v_d(t)$ and $\psi_d(t)$ are the desired reference signals assumed to be uniformly bounded and smooth, see Assumption 8 below. The secondary control objective is formalized as follows:

$$\lim_{t\to\infty} \left[\hat{V}_x(t) - V_x\right] = 0, \tag{2a}$$

$$\lim_{t\to\infty} \left[\hat{V}_y(t) - V_y\right] = 0\,, \tag{2b}$$

where $\hat{V}_x$ and $\hat{V}_y$ are the estimates of V_x and V_y, respectively. Finally, the following assumption is introduced:

Assumption 8: The reference signals $u_d(t)$, $v_d(t)$ and $\psi_d(t)$ are uniformly bounded class C^2 functions.

Remark 5: Assumption 8 does not represent a limitation for any practical implementation since all the reference signals can be considered, in practice, to be continuous, bounded and differentiable.

III. First Control Plant Model and Controller C1

A. First Control Plant Model

Under Assumption 5 one can employ low-speed maneuvering models for control design purposes. Such models are similar to DP models [36], [38], but instead of modeling the disturbance using a force vector, the relative velocity is used in the low-speed approach. The first control plant model relies, in addition to the aforementioned assumptions, on two other assumptions:

Assumption 9: The desired heading ψ_d is slowly varying and the vehicle experiences very low rotation rates r, i.e. $|r| < 0.05$ rad/s ≈ 3 deg/s. Therefore, the Coriolis-centripetal forces are neglected, and $\dot{\psi}_d \approx 0$.

Remark 6: Assumption 9 is valid in a regime where the ROV performs smooth maneuvers, such as when the vehicle is required to follow a flat net pen [35], strengthened by the fact that the ROV is assumed to maneuver at low speeds (Assumption 5).

Following Assumptions 1-9, the 3-DOF control plant maneuvering model of the ROV, which is adequate for slow-speed maneuvering tasks, is given by the equations

$$\dot{\boldsymbol{\eta}}^n = \boldsymbol{R}(\psi)\boldsymbol{\nu}^b \tag{3a}$$

$$\boldsymbol{M}_{RB}\dot{\boldsymbol{\nu}}^b + \boldsymbol{M}_A\dot{\boldsymbol{\nu}}_r^b + \boldsymbol{D}\boldsymbol{\nu}_r^b = \boldsymbol{\tau}_{C1}\,, \tag{3b}$$

where $\boldsymbol{\eta}^n, \boldsymbol{\nu}^b \in \mathbb{R}^3$ and the matrix $\boldsymbol{R}(\psi) \in \mathbb{R}^{3\times 3}$ is the principal rotation matrix around the z-axis. In addition, $\boldsymbol{\nu}_r^b \triangleq \boldsymbol{\nu}^b - \boldsymbol{\nu}_c^b$ is the relative velocity vector of the vehicle with respect to the ocean current. In the frame $\{b\}$, the current velocity is

$$\boldsymbol{\nu}_c^b = \boldsymbol{R}^\top(\psi)\mathbf{V}_c^n = \begin{bmatrix} u_c & v_c & 0 \end{bmatrix}^\top. \tag{4}$$

The matrices $\boldsymbol{M}_{RB} = \boldsymbol{M}_{RB}^\top > 0 \in \mathbb{R}^{3\times 3}$ and $\boldsymbol{M}_A = \boldsymbol{M}_A^\top > 0 \in \mathbb{R}^{3\times 3}$ describe the rigid-body inertia and the added mass, respectively, while $\boldsymbol{D} > 0 \in \mathbb{R}^{3\times 3}$ is the damping matrix. The matrices $\boldsymbol{R}(\psi), \boldsymbol{M}_{RB}, \boldsymbol{M}_A$ and $\boldsymbol{D}$ are as follows:

$$\boldsymbol{R}(\psi) \triangleq \begin{bmatrix} \cos(\psi) & -\sin(\psi) & 0 \\ \sin(\psi) & \cos(\psi) & 0 \\ 0 & 0 & 1 \end{bmatrix}, \tag{5a}$$

$$\boldsymbol{M}_i \triangleq \begin{bmatrix} m_{11}^i & 0 & 0 \\ 0 & m_{22}^i & 0 \\ 0 & 0 & m_{33}^i \end{bmatrix}, \quad \boldsymbol{D} \triangleq \begin{bmatrix} d_{11} & 0 & 0 \\ 0 & d_{22} & 0 \\ 0 & 0 & d_{33} \end{bmatrix}, \tag{5b}$$

where $i \in \{RB, A\}$. The control forces and moments acting on the vehicle are collected in the vector

$$\boldsymbol{\tau}_{C1} = \begin{bmatrix} \tau_{C1,u} & \tau_{C1,v} & \tau_{C1,r} \end{bmatrix}^\top \tag{6}$$

and the following assumption is introduced

Assumption 10: Thruster failures are not considered and the ROV is fully actuated at all times.

B. First Control Plant Model in Component Form

To solve the control design problem it is useful to expand the kinematic and kinetic equations, (3a) and (3b), into their component forms. The time-derivative of the current velocity vector in $\{b\}$, (4) is

$$\dot{\boldsymbol{\nu}}_c^b = \frac{\mathrm{d}}{\mathrm{d}t}\left(\boldsymbol{R}^\top(\psi)\mathbf{V}_c^n\right) = \begin{bmatrix} rv_c & -ru_c & 0 \end{bmatrix}^\top, \tag{7}$$

the 3-DOF control plant model may be written as

$$\dot{x} = u\cos(\psi) - v\sin(\psi), \tag{8a}$$

$$\dot{y} = u\sin(\psi) + v\cos(\psi), \tag{8b}$$

$$\dot{\psi} = r, \tag{8c}$$

$$\dot{u} = -\frac{d_{11}}{m_{11}}u + \boldsymbol{\phi}_u^\top\bar{\mathbf{V}}_c^n + \frac{1}{m_{11}}\tau_{C1,u}, \tag{8d}$$

$$\dot{v} = -\frac{d_{22}}{m_{22}}v + \boldsymbol{\phi}_v^\top\bar{\mathbf{V}}_c^n + \frac{1}{m_{22}}\tau_{C1,v}, \tag{8e}$$

$$\dot{r} = -\frac{d_{33}}{m_{33}}r + \frac{1}{m_{33}}\tau_{C1,r}\,, \tag{8f}$$

where $m_{ii} \triangleq m_{ii}^{RB} + m_{ii}^A$, $\bar{\mathbf{V}}_c^n = \begin{bmatrix} V_x & V_y \end{bmatrix}^\top$, and

$$\boldsymbol{\phi}_u = \begin{bmatrix} \frac{d_{11}}{m_{11}}\cos(\psi) - \frac{m_{11}^A}{m_{11}}r\sin(\psi) \\ \frac{d_{11}}{m_{11}}\sin(\psi) + \frac{m_{11}^A}{m_{11}}r\cos(\psi) \end{bmatrix}, \tag{9a}$$

$$\boldsymbol{\phi}_v = \begin{bmatrix} -\frac{d_{22}}{m_{22}}\sin(\psi) - \frac{m_{22}^A}{m_{22}}r\cos(\psi) \\ \frac{d_{22}}{m_{22}}\cos(\psi) - \frac{m_{22}^A}{m_{22}}r\sin(\psi) \end{bmatrix}. \tag{9b}$$

C. Surge, Sway and Yaw Control for the First Model

This part presents the controller C1 that achieves the primary and secondary control objectives (1) and (2). Its derivation is based on the control plant model given by (3a) and (3b).

First, a heading controller able to track the desired heading $\psi_d(t)$ is proposed. Let

$$\tau_{C1,r} = m_{33}\dot{r}_d(t) + d_{33}r_d(t) - k_{p,\psi}\tilde{\psi} - k_{d,\psi}\tilde{r}, \tag{10}$$

where $k_{p,\psi}$ and $k_{d,\psi} > 0$ are constant controller gains, m_{33}, $d_{33} > 0$, and we introduced the closed-loop states $\tilde{\psi} := \psi - \psi_d(t)$ and $\tilde{r} := r - r_d(t)$. After Assumption 8, $r_d(t) = \dot{\psi}_d(t)$ is bounded and smooth. $\tau_{C1,r}$ above is a PD-controller with reference feedforward, designed to steer $r \to r_d(t)$ and $\psi \to \psi_d(t)$. More precisely, we have the following.

Lemma 1: With d_{33}, $k_{d,\psi}$, $k_{p,\psi}$, $m_{33} > 0$, and if assumptions 1-8 hold, the origin of the closed-loop subsystem for yaw, resulting from (8f) and (10):

$$\dot{\tilde{r}} = -\left(\frac{d_{33} + k_{d,\psi}}{m_{33}}\right)\tilde{r} - \frac{k_{p,\psi}}{m_{33}}\tilde{\psi}, \tag{11a}$$

$$\dot{\tilde{\psi}} = \tilde{r} \tag{11b}$$

is uniformly globally exponentially stable (UGES).

Proof: The eigenvalues of the subsystem, which is linear in $\tilde{r}$ and $\tilde{\psi}$, can be calculated by finding the zeros of the characteristic equation:

$$\lambda^2 + \frac{d_{33} + k_{d,\psi}}{m_{33}}\lambda + \frac{k_{p,\psi}}{m_{33}} = 0\,. \tag{12}$$

The eigenvalues are strictly negative for all gains $k_{d,\psi}, k_{p,\psi} > 0$, and the solution will thus converge uniformly and exponentially to the origin for any initial values $\tilde{r}(0) = \tilde{r}_0$ and $\tilde{\psi}(0) = \tilde{\psi}_0$. ∎

Next, we introduce the velocity controller. Given the desired velocities $u_d(t)$ and $v_d(t)$ let $\boldsymbol{v}_d = \begin{bmatrix} u_d & v_d \end{bmatrix}^\top$ and $\boldsymbol{v} = \begin{bmatrix} u & v \end{bmatrix}^\top$ and let us define the error state variables:

$$\boldsymbol{z}_1 := \boldsymbol{v} - \boldsymbol{v}_d \tag{13}$$

$$\boldsymbol{z}_2 := \bar{\mathbf{V}}_c^n - \hat{\bar{\mathbf{V}}}_c^n\,, \tag{14}$$

where $\hat{\bar{\mathbf{V}}}_c^n = \begin{bmatrix} \hat{V}_x & \hat{V}_y \end{bmatrix}^\top$ is the estimate of the actual ocean current velocity $\bar{\mathbf{V}}_c^n$. Then, the following controller is proposed:

$$Z\bar{\boldsymbol{\tau}}_{C1} = \boldsymbol{D}_2\boldsymbol{v}_d + \boldsymbol{M}_2\left(\dot{\boldsymbol{v}}_d - \boldsymbol{K}_p\boldsymbol{z}_1 - \boldsymbol{G}(t)\hat{\bar{\mathbf{V}}}_c^n\right) \tag{15}$$

$$\dot{\hat{\bar{\mathbf{V}}}}_c^n = \boldsymbol{\Gamma}\boldsymbol{G}(t)^\top\boldsymbol{z}_1, \tag{16}$$

where

$$\boldsymbol{M}_2 = \begin{bmatrix} m_{11} & 0 \\ 0 & m_{22} \end{bmatrix} \tag{17}$$

$$\boldsymbol{D}_2 = \begin{bmatrix} d_{11} & 0 \\ 0 & d_{22} \end{bmatrix} \tag{18}$$

$$\boldsymbol{K}_p = \begin{bmatrix} k_{p,u} & 0 \\ 0 & k_{p,v} \end{bmatrix} \tag{19}$$

$$\boldsymbol{G}(t) = \begin{bmatrix} \frac{d_{11}}{m_{11}}\cos(\psi_d(t)) & \frac{d_{11}}{m_{11}}\sin(\psi_d(t)) \\ -\frac{d_{22}}{m_{22}}\sin(\psi_d(t)) & \frac{d_{22}}{m_{22}}\cos(\psi_d(t)) \end{bmatrix}, \tag{20}$$

$k_{p,u}$, $k_{p,v} > 0$ are constant control gains, and the matrix $\boldsymbol{\Gamma} = \boldsymbol{\Gamma}^\top > 0 \in \mathbb{R}^{2\times 2}$ is a diagonal matrix containing the constant adaption gains to update $\hat{\bar{\mathbf{V}}}_c^n$.

D. Stability Analysis for Controller C1

The closed-loop system corresponding to the velocities is obtained by differentiating on both sides of (13) and (14). For the latter, since the current $\bar{\mathbf{V}}_c^n$ is constant (Assumption 7), we have

$$\dot{\boldsymbol{z}}_2 = -\dot{\hat{\bar{\mathbf{V}}}}_c^n, \tag{21}$$

Then, we can use (16). On the other hand, we split $\bar{\boldsymbol{\tau}}_{C1}$ in (15) as $\bar{\boldsymbol{\tau}}_{C1} =: \begin{bmatrix} \tau_{C1,u} & \tau_{C1,v} \end{bmatrix}^\top$ and we use (15) and (17)–(20) to find the explicit expressions of $\tau_{C1,u}$ and $\tau_{C1,v}$, and use them in (8d) and (8e). Thus, we obtain

$$\dot{\boldsymbol{z}}_1 = -(\boldsymbol{M}_2^{-1}\boldsymbol{D}_2 + \boldsymbol{K}_p)\boldsymbol{z}_1 + \boldsymbol{G}(t)\boldsymbol{z}_2 + \boldsymbol{g}(\boldsymbol{\theta}, t)\boldsymbol{\theta}, \tag{22}$$

$$\dot{\boldsymbol{z}}_2 = -\boldsymbol{\Gamma}\boldsymbol{G}(t)^\top\boldsymbol{z}_1 \tag{23}$$

where $\boldsymbol{\theta} \triangleq \begin{bmatrix} \tilde{r} & \tilde{\psi} \end{bmatrix}^\top$ and $\boldsymbol{g}(\boldsymbol{\theta}, t)$ is a bounded function describing the influence of $\boldsymbol{\theta}$ on the velocity states. The explicit definition of $\boldsymbol{g}(\boldsymbol{\theta}, t)$ is given in Appendix A.

It is important to remark that the overall closed-loop system, given by Equations (10) and (22)-(23) has a cascaded form. Since the interconnection term $\boldsymbol{g}(\boldsymbol{\theta}, t)$ is independent of $\boldsymbol{z}$ and uniformly bounded in t, and the $\boldsymbol{\theta}$-dynamics is UGES (Lemma 1), with the purpose of invoking a cascades argument (see Theorem 1 farther below) we establish next that the origin is UGAS for (22)-(23).

Consider an unperturbed version of the system described by (22) and (23), i.e., omitting the term $\boldsymbol{g}(\boldsymbol{\theta}, t)\boldsymbol{\theta}$.

Lemma 2: With $\boldsymbol{M}_2$, $\boldsymbol{D}_2$, $\boldsymbol{K}_p$ and $\boldsymbol{G}(t)$ as in (17)-(20), respectively, $\boldsymbol{\Gamma} = \boldsymbol{\Gamma}^\top > 0 \in \mathbb{R}^{2\times 2}$, and under Assumptions 1-8 the origin of the unperturbed closed loop velocity error system given by

$$\dot{\tilde{\boldsymbol{v}}} = -(\boldsymbol{M}_2^{-1}\boldsymbol{D}_2 + \boldsymbol{K}_p)\tilde{\boldsymbol{v}} + \boldsymbol{G}(t)\tilde{\bar{\mathbf{V}}}_c^n \tag{24a}$$

$$\dot{\tilde{\bar{\mathbf{V}}}}_c^n = -\boldsymbol{\Gamma}\boldsymbol{G}(t)^\top\tilde{\boldsymbol{v}} \tag{24b}$$

is UGAS and ULES.

Proof: Consider the nominal system obtained from (24a) by discarding the term $\boldsymbol{G}(t)\tilde{\bar{\mathbf{V}}}_c^n$:

$$\dot{\tilde{\boldsymbol{v}}} = -(\boldsymbol{M}_2^{-1}\boldsymbol{D}_2 + \boldsymbol{K}_p)\tilde{\boldsymbol{v}}. \tag{25}$$

It is first shown that (25) is UGES. Consider the positive definite radially unbounded Lyapunov function candidate:

$$k_1\|\tilde{\boldsymbol{v}}\|^2 \leq V(\tilde{\boldsymbol{v}}) = \frac{1}{2}\tilde{\boldsymbol{v}}^\top\tilde{\boldsymbol{v}} \leq k_2\|\tilde{\boldsymbol{v}}\|^2\,. \tag{26}$$

It can be shown that there exists a $k_3 > 0$ such that:

$$\dot{V}(\tilde{\boldsymbol{v}}) = -\tilde{\boldsymbol{v}}^\top(\boldsymbol{M}_2^{-1}\boldsymbol{D}_2 + \boldsymbol{K}_p)\tilde{\boldsymbol{v}} \leq k_3\|\tilde{\boldsymbol{v}}\|^2\,. \tag{27}$$

This is due to the fact that $\boldsymbol{M}_2$, $\boldsymbol{D}_2$ and $\boldsymbol{K}_p$ are positive definite matrices. Then, by applying [25, Thm. 4.10] the origin of the nominal system is UGES. Furthermore, we have

$$\begin{aligned} &\boldsymbol{G}(t)^\top\boldsymbol{G}(t) = \\ &\begin{bmatrix} a_1\cos^2(\psi_d) + a_2\sin^2(\psi_d) & a_3\cos(\psi_d)\sin(\psi_d) \\ a_3\cos(\psi_d)\sin(\psi_d) & a_1\sin^2(\psi_d) + a_2\cos^2(\psi_d) \end{bmatrix} \\ &\geq b_m\mathbf{I}\,, \end{aligned} \tag{28}$$

where $b_m > 0$ and

$$a_1 = \left(\frac{d_{11}}{m_{11}}\right)^2 \tag{29}$$

$$a_2 = \left(\frac{d_{22}}{m_{22}}\right)^2 \tag{30}$$

$$a_3 = \left(\frac{d_{11}}{m_{11}}\right)^2 - \left(\frac{d_{22}}{m_{22}}\right)^2\,. \tag{31}$$

The last inequality in (28) follows from the fact that the principle minors of $\boldsymbol{G}(t)^\top\boldsymbol{G}(t)$ are strictly positive. Indeed, on one hand, $a_1\cos^2(\psi_d) + a_2\sin^2(\psi_d) \geq \min\{a_1, a_2\}$ while the determinant of this matrix satisfies

$$\begin{aligned} &|\boldsymbol{G}^\top\boldsymbol{G}| \\ &= \left(a_1\cos^2(\psi_d) + a_2\sin^2(\psi_d)\right)\left(a_1\sin^2(\psi_d) + a_2\cos^2(\psi_d)\right) \\ &\quad - a_3^2\sin^2(\psi_d)\cos^2(\psi_d) \\ &= a_1a_2[\sin^4(\psi_d) + 2\cos^2(\psi_d)\sin^2(\psi_d) + \cos^4(\psi_d)] \\ &= a_1a_2(\sin^2(\psi_d) + \cos^2(\psi_d))^2 \\ &= a_1a_2 > 0\,. \end{aligned} \tag{32}$$

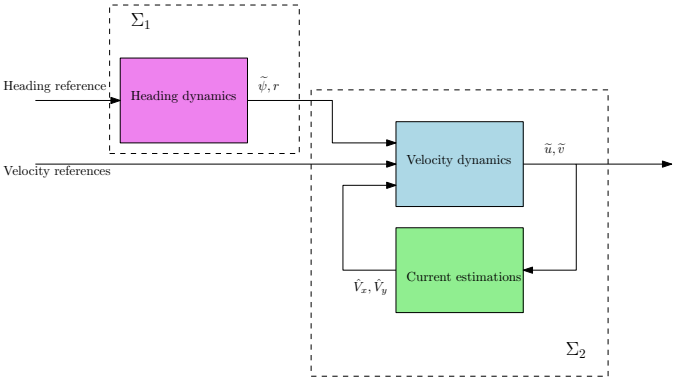

Fig. 2: The cascaded system

For the second equality above we completed the squares using the values given for a_1, a_2 and a_3 in (29)-(31). Therefore, all the assumptions of [12, Thm. 1] are satisfied and UGAS and ULES for the origin of the system (22) and (23) follows. ■

From the previous Lemmata we obtain the following.

Theorem 1: The origin of the heading error system with the controller from (10), in cascade with the velocity error system of (22) with the adaptive laws given in (23) is UGAS and ULES under Assumption 1-10 for the control plant model (8).

Proof: Define $\boldsymbol{x_1} \triangleq \begin{bmatrix} \tilde{r} & \tilde{\psi} \end{bmatrix}^\top$ and $\boldsymbol{x_2} \triangleq \begin{bmatrix} \tilde{\boldsymbol{v}} & \tilde{\boldsymbol{V}}_c \end{bmatrix}^\top$. Then,

$$\Sigma_1 : \dot{\boldsymbol{x}}_1 = f_1(t, \boldsymbol{x_1}) \,, \tag{33}$$

$$\Sigma_2 : \dot{\boldsymbol{x}}_2 = f_2(t, \boldsymbol{x_2}) + \boldsymbol{g}(\boldsymbol{\theta}, t)\boldsymbol{x_1} \,. \tag{34}$$

The origin $\{x_1 = 0\}$ is shown to be UGES for Σ_1. Furthermore, the interconnection term $\boldsymbol{g}(t)$ is bounded elementwise by application of L'Hôpital's rule [39], see Appendix A. As such the cascaded system (Σ_1, Σ_2) given by (33)-(34) and shown in Figure 2 satisfies the assumptions required for applications of [40, Thm. 2] and the cascaded system (Σ_1, Σ_2) is UGAS. Furthermore, both (33) and (34) satisfy conditions for κ-exponential stability as defined in [41, Def. 2.2.9] and as such, by [42, Lemma 8] the cascaded system (Σ_1, Σ_2) is κ-exponentially stable, i.e., UGAS and ULES and the origin $\{x_2 = 0\}$ is shown to be UGAS for $\dot{\boldsymbol{x}}_2 = f_2(t, \boldsymbol{x}_2)$.

■

This means that the proposed controller C1 achieves the primary control objectives (1) as well as the secondary control objectives (2) with UGAS and ULES properties.

IV. Second Control Plant Model and Controller C2

A. Second Control Plant Model

The first control plant model does not consider the Coriolis-centripetal forces, which may arise when the ROV performs more aggressive maneuvers to avoid obstacles or attempts to follow a net with sharp bends and corners [35]. Therefore the second control plant model omits Assumption 9 and expands the first control plant model to also consider the nonlinear Coriolis-centripetal term. The maneuvering model of the 3-DOF ROV then becomes:

$$\dot{\boldsymbol{\eta}} = \boldsymbol{R}(\psi)\boldsymbol{\nu} \tag{35a}$$

$$\boldsymbol{M}_{RB}\dot{\boldsymbol{\nu}} + \boldsymbol{M}_A\dot{\boldsymbol{\nu}}_r + \boldsymbol{D}\boldsymbol{\nu}_r + \boldsymbol{C}_{RB}(\boldsymbol{\nu})\boldsymbol{\nu} + \boldsymbol{C}_A(\boldsymbol{\nu}_r)\boldsymbol{\nu}_r = \boldsymbol{\tau}_{C2}, \tag{35b}$$

where the matrices and vectors are as defined in (5a), (5b) and (6), u_r and v_r are the relative surge and sway velocities, respectively, and

$$\boldsymbol{C}_{RB}(\boldsymbol{\nu}) = \begin{bmatrix} 0 & 0 & -m_{22}^{RB}v \\ 0 & 0 & m_{11}^{RB}u \\ m_{22}^{RB}v & -m_{11}^{RB}u & 0 \end{bmatrix} \tag{36}$$

$$\boldsymbol{C}_A(\boldsymbol{\nu}_r) = \begin{bmatrix} 0 & 0 & -m_{22}^{A}v_r \\ 0 & 0 & m_{11}^{A}u_r \\ m_{22}^{A}v_r & -m_{11}^{A}u_r & 0 \end{bmatrix} \tag{37}$$

represent the rigid body and added mass Coriolis and centripetal forces, respectively.

The model, in its component form, becomes:

$$\dot{x} = u\cos(\psi) - v\sin(\psi), \tag{38a}$$

$$\dot{y} = u\sin(\psi) + v\cos(\psi), \tag{38b}$$

$$\dot{\psi} = r, \tag{38c}$$

$$m_{11}\dot{u} + (m_{11}^A - m_{22}^A)r(V_x\sin(\psi) - V_y\cos(\psi)) + d_{11}(u - V_x\cos(\psi) - V_y\sin(\psi)) - m_{22}vr = \tau_{C2,u}\,, \tag{38d}$$

$$m_{22}\dot{v} - (m_{11}^A - m_{22}^A)r(V_x\cos(\psi) + V_y\sin(\psi)) + d_{22}(v + V_x\sin(\psi) - V_y\cos(\psi)) + m_{11}ur = \tau_{C2,v}\,, \tag{38e}$$

$$m_{33}\dot{r} + d_{33}r + (m_{22} - m_{11})uv - (m_{11}^A - m_{22}^A)\boldsymbol{v}^\top\boldsymbol{\phi}(\psi)\bar{\mathbf{V}}_c^n + \frac{1}{2}(m_{11}^A - m_{22}^A)\bar{\mathbf{V}}_c^{n\top}\boldsymbol{\phi}(2\psi)\bar{\mathbf{V}}_c^n = \tau_{C2,r}, \tag{38f}$$

where $\bar{\mathbf{V}}_c^n \triangleq \begin{bmatrix} V_x & V_y \end{bmatrix}^\top$, $\boldsymbol{v} \triangleq \begin{bmatrix} u & v \end{bmatrix}^\top$, and

$$\boldsymbol{\phi}(\,\cdot\,) \triangleq \begin{bmatrix} \sin(\,\cdot\,) & -\cos(\,\cdot\,) \\ -\cos(\,\cdot\,) & -\sin(\,\cdot\,) \end{bmatrix} . \tag{39}$$

B. Surge, Sway and Yaw Control for the Second Model

In this section the controller C2 for the 3-DOF control plant model given by (35a) and (35b) is proposed. The controller C2 achieves the primary control objective as follows:

$$\begin{aligned} \boldsymbol{\tau}_{C2} =& \boldsymbol{M}\dot{\boldsymbol{\nu}}_d + \boldsymbol{D}\boldsymbol{\nu}_d + \boldsymbol{s} + \hat{\boldsymbol{a}} \\ & - \boldsymbol{M}\boldsymbol{K}\tilde{\boldsymbol{\nu}}_{\text{aug}} - \boldsymbol{M}_{\text{aug}}\boldsymbol{G}_{C2}(\boldsymbol{\nu}_{\text{aug}}, t)\hat{\bar{\mathbf{V}}}_c^n \,, \end{aligned} \tag{40}$$

where $\boldsymbol{M} \triangleq \boldsymbol{M}_{RB} + \boldsymbol{M}_A$, $\boldsymbol{\nu}_d = \begin{bmatrix} u_d & v_d & r_d \end{bmatrix}^\top$, $\dot{\boldsymbol{\nu}}_d = \begin{bmatrix} \dot{u}_d & \dot{v}_d & \dot{r}_d \end{bmatrix}^\top$. The vector $\tilde{\boldsymbol{\nu}}_{\text{aug}}$ is defined as:

$$\tilde{\boldsymbol{\nu}}_{\text{aug}} = \begin{bmatrix} \tilde{u} & \tilde{v} & \tilde{r} & \tilde{\psi} \end{bmatrix}^\top , \tag{41}$$

where $\tilde{u} = u - u_d$, $\tilde{v} = v - v_d$, $\tilde{r} = r - r_d$ and $\tilde{\psi} = \psi - \psi_d$. A feedback linearizing term, $\boldsymbol{s}$, and a vector for

handling unknown quadratic terms arising in this model, $\hat{\boldsymbol{a}}$, are introduced. These terms are defined as:

$$\boldsymbol{s} \triangleq \begin{bmatrix} -m_{22}vr \\ m_{11}ur \\ (m_{22}-m_{11})uv \end{bmatrix}, \tag{42}$$

$$\hat{\boldsymbol{a}} \triangleq \begin{bmatrix} 0 \\ 0 \\ (m^A_{22}-m^A_{11})\boldsymbol{\alpha}_e^\top \hat{\boldsymbol{e}} \end{bmatrix}, \tag{43}$$

where:

$$\boldsymbol{\alpha}_e = \begin{bmatrix} -\frac{1}{2}\sin(2\psi) \\ \cos(2\psi) \\ \frac{1}{2}\sin(2\psi) \end{bmatrix}, \quad \hat{\boldsymbol{e}} = \begin{bmatrix} \widehat{V_x^2} \\ \widehat{V_xV_y} \\ \widehat{V_y^2} \end{bmatrix}. \tag{44}$$

The matrices are defined as in (5b), in addition to:

$$\boldsymbol{M}_{\text{aug}} \triangleq \begin{bmatrix} m_{11} & 0 & 0 & 0 \\ 0 & m_{22} & 0 & 0 \\ 0 & 0 & m_{33} & 0 \end{bmatrix}, \tag{45}$$

$$\boldsymbol{K} \triangleq \begin{bmatrix} k_{p_u} & 0 & 0 & 0 \\ 0 & k_{p_v} & 0 & 0 \\ 0 & 0 & k_{d_\psi} & k_{p_\psi} \end{bmatrix}, \tag{46}$$

$$\boldsymbol{G}_{C2}(\boldsymbol{\nu}_{\text{aug}}, t) := \begin{bmatrix} g_{C2,11} & g_{C2,12} \\ g_{C2,21} & g_{C2,22} \\ g_{C2,31} & g_{C2,32} \\ 0 & 0 \end{bmatrix}, \tag{47}$$

where the elements of the $\boldsymbol{G}_{C2}(\boldsymbol{\nu}_{\text{aug}}, t)$ are defined as:

$$g_{C2,11} = \frac{m^A_{22}-m^A_{11}}{m_{11}} r\sin(\psi) + \frac{d_{11}}{m_{11}}\cos(\psi), \tag{48a}$$

$$g_{C2,12} = -\frac{m^A_{22}-m^A_{11}}{m_{11}} r\cos(\psi) + \frac{d_{11}}{m_{11}}\sin(\psi), \tag{48b}$$

$$g_{C2,21} = -\frac{m^A_{22}-m^A_{11}}{m_{22}} r\cos(\psi) - \frac{d_{22}}{m_{22}}\sin(\psi), \tag{48c}$$

$$g_{C2,22} = -\frac{m^A_{22}-m^A_{11}}{m_{22}} r\sin(\psi) + \frac{d_{22}}{m_{22}}\cos(\psi), \tag{48d}$$

$$g_{C2,31} = -\frac{m^A_{22}-m^A_{11}}{m_{33}} (u\sin(\psi) - v\cos(\psi)), \tag{48e}$$

$$g_{C2,32} = \frac{m^A_{22}-m^A_{11}}{m_{33}} (u\cos(\psi) + v\sin(\psi)). \tag{48f}$$

Remark 7: The terms above depend on $\boldsymbol{\nu}_{\text{aug}}$ and t through $\psi = \tilde{\psi} + \psi_d(t)$—see (41), but these arguments are not made explicit to avoid a cumbersome notation.

The estimate for $\hat{\bar{\mathbf{V}}}_c^n$ is governed by the following update law:

$$\dot{\hat{\bar{\mathbf{V}}}}_c^n = \boldsymbol{\Gamma}_1 \boldsymbol{G}_{C2}(\boldsymbol{\nu}_{\text{aug}}, t)^\top \left(\frac{\partial W(\tilde{\boldsymbol{\nu}}_{\text{aug}})}{\partial \boldsymbol{\nu}_{\text{aug}}} \right)^\top \tag{49}$$

where $W : \mathbb{R}^4 \to \mathbb{R}$ is a class C^1 function satisfying properties as in [12] that is function is given explicitly farther below. Given $\tilde{\boldsymbol{e}} \triangleq [V_x^2 \;\; V_xV_y \;\; V_y^2]^\top - \hat{\boldsymbol{e}}$ and due to Assumption 7, $\dot{\tilde{\boldsymbol{e}}} = -\dot{\hat{\boldsymbol{e}}}$. As such the error variable containing the quadratic terms, $\hat{\boldsymbol{e}}$, is updated using:

$$\dot{\hat{\boldsymbol{e}}} = -\frac{m^A_{22}-m^A_{11}}{m_{33}} \boldsymbol{\Gamma}_2 \boldsymbol{\alpha}_e (m_{33}\tilde{r} + \epsilon\tilde{\psi}). \tag{50}$$

The matrices $\boldsymbol{\Gamma}_1 \in \mathbb{R}^{2\times 2}$ and $\boldsymbol{\Gamma}_2 \in \mathbb{R}^{3\times 3}$ are positive definite, diagonal tuning matrices. In addition the tuning parameter ϵ is chosen such that:

$$0 < \epsilon < \min\left\{ \frac{d_{33}k_{p_\psi} + m_{33}k_{p_\psi}k_{d_\psi}}{k_{p_\psi} + \frac{1}{4}\left(\frac{d_{33}}{m_{33}} + k_{d_\psi}\right)}, m_{33}\sqrt{k_{p_\psi}} \right\} \tag{51}$$

C. Stability Analysis for Controller C2

The stability analysis for controller C2 given by (40) is provided here and shows that the closed-loop system of (35a) and (35b) with the proposed controller C2 converges to zero for $\tilde{\boldsymbol{\nu}}_{\text{aug}}$. The matrices and vectors are as in Section IV-B.

The closed-loop system describing the ROV is first presented in terms of the error variable given in (41). Consider the following positive definite, radially unbounded function

$$W(\tilde{\boldsymbol{\nu}}_{\text{aug}}) \triangleq \frac{1}{2}\tilde{\boldsymbol{\nu}}_{\text{aug}}^\top \boldsymbol{P}\tilde{\boldsymbol{\nu}}_{\text{aug}} \tag{52}$$

where

$$\boldsymbol{P} = \begin{bmatrix} m_{11} & 0 & 0 & 0 \\ 0 & m_{22} & 0 & 0 \\ 0 & 0 & m_{33} & \epsilon \\ 0 & 0 & \epsilon & m_{33}k_{p_\psi} \end{bmatrix}, \tag{53}$$

and

$$\left(\frac{\partial W(\tilde{\boldsymbol{\nu}}_{\text{aug}})}{\partial \boldsymbol{\nu}_{\text{aug}}} \right)^\top = \begin{bmatrix} m_{11}\tilde{u} \\ m_{22}\tilde{v} \\ m_{33}\tilde{r} + \epsilon\tilde{\psi} \\ m_{33}k_{p_\psi}\tilde{\psi} + \epsilon\tilde{r} \end{bmatrix}. \tag{54}$$

Inserting the control law (40) into (35b), and using error variables $\tilde{\boldsymbol{\nu}}_{\text{aug}}$ from (41), and

$$\tilde{\bar{\mathbf{V}}}_c^n = \bar{\mathbf{V}}_c^n - \hat{\bar{\mathbf{V}}}_c^n, \tag{55}$$

respectively, and

$$\tilde{\boldsymbol{e}} = \begin{bmatrix} V_xV_x - \widehat{V_xV_x} \\ V_xV_y - \widehat{V_xV_y} \\ V_yV_y - \widehat{V_yV_y} \end{bmatrix} \tag{56}$$

gives the closed-loop system of the ROV in the following form

$$\dot{\tilde{\boldsymbol{\nu}}}_{\text{aug}} = -\boldsymbol{A}\tilde{\boldsymbol{\nu}}_{\text{aug}} + \boldsymbol{\sigma}(\boldsymbol{v}, \tilde{\boldsymbol{e}}) + \boldsymbol{G}_{C2}(\boldsymbol{\nu}_{\mathbf{aug}}, t)\tilde{\bar{\mathbf{V}}}_c^n \tag{57}$$

where

$$\boldsymbol{A} \triangleq \begin{bmatrix} \frac{d_{11}}{m_{11}} + k_{p_u} & 0 & 0 & 0 \\ 0 & \frac{d_{22}}{m_{22}} + k_{p_v} & 0 & 0 \\ 0 & 0 & \frac{d_{33}}{m_{33}} + k_{d_\psi} & k_{p_\psi} \\ 0 & 0 & 1 & 0 \end{bmatrix} \tag{58}$$

and

$$\boldsymbol{\sigma}(\boldsymbol{v}, \tilde{\boldsymbol{e}}) \triangleq \begin{bmatrix} 0 \\ 0 \\ \frac{m^A_{11}-m^A_{22}}{m_{33}} \tilde{\boldsymbol{e}}^\top \boldsymbol{\alpha}_e \\ 0 \end{bmatrix} \tag{59}$$

Theorem 2: The origin of the full closed-loop system (57) with the adaptive laws (49) and (50) is UGS under Assumption 1-7, Assumption 10 and Assumption 8.

Proof: Choose the positive definite and radially unbounded Lyapunov function candidate

$$V(\tilde{\boldsymbol{\nu}}_{\text{aug}}, \tilde{\mathbf{V}}_c^n, \tilde{\boldsymbol{e}}) = W(\tilde{\boldsymbol{\nu}}_{\text{aug}}) + \frac{1}{2}\tilde{\mathbf{V}}_c^{n\top}\boldsymbol{\Gamma}_1^{-1}\tilde{\mathbf{V}}_c^n + \frac{1}{2}\tilde{\boldsymbol{e}}^\top\boldsymbol{\Gamma}_2^{-1}\tilde{\boldsymbol{e}} \tag{60}$$

with $W(\tilde{\boldsymbol{\nu}}_{\text{aug}})$ as defined in (52), and $\tilde{\mathbf{V}}_c^n$ and $\tilde{\boldsymbol{e}}$ as in (55) and (56), respectively. Further, $\boldsymbol{\Gamma}_1 = \boldsymbol{\Gamma}_1^\top > 0 \in \mathbb{R}^{2\times 2}$ and $\boldsymbol{\Gamma}_2 = \boldsymbol{\Gamma}_2^\top > 0 \in \mathbb{R}^{3\times 3}$.

The time derivative of (60) along the trajectories of the system (57), with the chosen adaptive laws (49) and (50) inserted, results in (with a slight abuse of notation)

$$\dot{V} = -\tilde{\boldsymbol{\nu}}_{\text{aug}}^\top \boldsymbol{H}\tilde{\boldsymbol{\nu}}_{\text{aug}} \tag{61}$$

where

$$\boldsymbol{H} = \begin{bmatrix} \boldsymbol{H}_1 & \mathbf{0}_{2\times 2} \\ \mathbf{0}_{2\times 2} & \boldsymbol{H}_2 \end{bmatrix} \tag{62}$$

with $\boldsymbol{H}_1 = \text{diag}\{d_{11} + m_{11}k_{p_u}, d_{22} + m_{22}k_{p_v}\}$ and

$$\boldsymbol{H}_2 = \begin{bmatrix} d_{33} + m_{33}k_{d_\psi} - \epsilon & \frac{1}{2}\epsilon(\frac{d_{33}}{m_{33}} + k_{d_\psi}) \\ \frac{1}{2}\epsilon(\frac{d_{33}}{m_{33}} + k_{d_\psi}) & k_{p_\psi}\epsilon \end{bmatrix}. \tag{63}$$

By application of Sylvester's criterion, the matrix $\boldsymbol{H}$ is positive definite. Furthermore, ϵ is chosen such that the bounds in (51) hold. Thus, the origin of the closed-loop system (57) is uniformly stable, according to [25, Thm. 4.8]. Furthermore, since (60) is radially unbounded, the origin is globally uniformly stable. ∎

Corollary 1: The error term $\tilde{\boldsymbol{\nu}}_{\text{aug}}$ converges to zero.

Proof: Consider the time derivative of (61) along it's trajectories

$$\ddot{V} = -2\tilde{\boldsymbol{\nu}}_{\text{aug}}^\top \boldsymbol{H}\dot{\tilde{\boldsymbol{\nu}}}_{\text{aug}}\,, \tag{64}$$

where all signals are bounded as a consequence of the UGS property of Theorem 2. As such $V(\tilde{\boldsymbol{\nu}}_{\text{aug}}, \tilde{\mathbf{V}}_c^n, \tilde{\boldsymbol{e}})$ is lower bounded and $\dot{V}(\tilde{\boldsymbol{\nu}}_{\text{aug}}, \tilde{\mathbf{V}}_c^n, \tilde{\boldsymbol{e}})$ is negative semi-definite and uniformly continuous. Through applications of Barbălat's lemma [43, Ch. 4.5.2] $\dot{V}(\tilde{\boldsymbol{\nu}}_{\text{aug}}, \tilde{\mathbf{V}}_c^n, \tilde{\boldsymbol{e}}) \to 0$ and thus $\tilde{\boldsymbol{\nu}}_{\text{aug}} \to 0$ as $t \to \infty$ is ensured. ∎

This means that the second control law achieves the primary control objective (1).

V. Simulation and Experimental Setup

A. Path Following Algorithm

In order to traverse a net pen the guidance law from [8] is used. This algorithm generates a desired heading angle, as well as desired velocities in the surge and sway DOF which assures that objective of following the net pen is achieved.

B. Reference Model

The reference model smooths out signals in order to avoid bandwidth problems in the control system. In addition, the reference model provides reference values for higher-order reference terms, e.g., velocity and acceleration. A second-order low pass filter is proposed for the velocity references, smoothing out the reference velocity value and generating the desired acceleration. The velocity reference model used is given as [38, Ch. 10.2.1]

$$\begin{bmatrix} \ddot{u}_d \\ \ddot{v}_d \end{bmatrix} = -2\begin{bmatrix} \zeta_u\omega_u & 0 \\ 0 & \zeta_v\omega_v \end{bmatrix}\begin{bmatrix} \dot{u}_d \\ \dot{v}_d \end{bmatrix} - \begin{bmatrix} \omega_u^2 & 0 \\ 0 & \omega_v^2 \end{bmatrix}\begin{bmatrix} u_d - u_{\text{ref}} \\ v_d - v_{\text{ref}} \end{bmatrix} \tag{65}$$

where $\zeta_u, \zeta_v > 0$ are the relative damping ratios, $\omega_u, \omega_v > 0$ are the natural frequencies, and $u_{\text{ref}}, v_{\text{ref}}$ are the velocity in surge or sway calculated by the path following algorithm.

For the second controller, a third-order reference model for the heading angle was designed. This reference model provides reference values for yaw, yaw rate and yaw acceleration and is given by

$$\dddot{\psi}_d + (2\zeta_\psi + 1)\omega_\psi\ddot{\psi}_d + (2\zeta_\psi + 1)\omega_\psi^2\dot{\psi}_d + \omega_\psi^3\psi_d = \omega_\psi^3\psi_{\text{ref}} \tag{66}$$

where ζ_ψ is the relative damping ratio, ω_ψ is the natural frequency, and ψ_{ref} is the heading angle calculated by the path following algorithm.

VI. Simulation

The control plant model of the ROV for both C1 and C2, given in (3) and (35), respectively, as well as the controllers C1 (as given in (15) and (16)) and C2 (as given in (40), (49) and (50)) were implemented in the simulation software FhSim which is a software platform and framework for mathematical modeling and numerical simulation, with a focus on marine applications, developed at SINTEF Ocean [44], [45].

The matrices of (3) and (35) used in the simulations, and from which other required matrices are derived, are as follows

$$\boldsymbol{M}_{RB} = \text{diag}\,[90, 90, 13] \tag{67}$$

$$\boldsymbol{M}_A = \text{diag}\,[54, 72, 5.2] \tag{68}$$

$$\boldsymbol{D} = \text{diag}\,[250, 200, 15]\,. \tag{69}$$

The current velocity was set to $V_x = V_y = 0.1\text{m/s}$ in all simulations which implies $V_x^2 = V_y^2 = V_xV_y = 0.01\text{m/s}$.

The net pen was simulated using a model of a static circular net cage [46]. For the guidance law, the desired distance to the net was set to 3 m, while the desired speed U_d was set to 0.3m/s for C1 and 0.5m/s for C2. A higher velocity value was used for C2 in order to excite the coupling effects of the Coriolis-centripetal forces and thus make the control objective more challenging.

The parameters for both controllers used in the simulations are found in Table I. All parameters where found through trial and error where the aim was to achieve a smooth transient response with fast convergence and low overshoot.

A. Simulation Results

1) Controller 1: Figure 3 shows the simulation results using C1 as given in (15) and (16). The controller tracks the velocity references with very low error. The velocities of the ROV are shown in the top two plots in Figure 3 where the actual velocities are given in blue, and the red dashed lines represent the desired velocities from the reference model.

The estimated ocean currents are given in the third and fourth plots of Figure 3. The simulated ocean current was constant in the NED frame (dashed yellow and purple lines

TABLE I: Controller parameters used in simulations

Parameter	C1	C2
$\omega_{u,v}$	2	2
$\zeta_{u,v}$	1	1
$V_{\max}$	0.5	0.5
ϵ_{V_i}	0.2	0.2
γ_x	3.5	0.01
γ_y	3.0	0.01
$k_{p,u}$, $k_{p,v}$	4.0	5.0
$k_{p,\psi}$	15	46.6
$k_{d,\psi}$	0.1	14.0
ω_ψ	-	1.6
ζ_ψ	-	1.0
ϵ_ψ	-	0.1
$\gamma_{e,i}$	-	0.0001

in the third plot), but the effects of the current on the ROVs BODY frame (dashed yellow and purple lines in the fourth plot) varies as the ROV moves along the circular path. From the third plot it is clear that the estimated current velocity (solid blue and red lines) in the NED frame is accurately estimated. Further, from the fourth plot of Figure 3, it is clear that the effects of the current in the BODY frame (solid red and blue lines) are also accurately estimated.

As can be seen in the bottom plot of Figure 3 the heading controller given in (10) ensures that the actual heading angle (blue solid line) tracks the desired heading angle (red dashed line) accurately.

2) Controller 2: Figure 4 shows the simulation results using C2 as given in (40), (49) and (50). As can be seen from the top two plots of Figure 4 the controller accurately tracks the velocity references with very low error. The actual velocities are given in blue and the desired velocities are given as red dashed lines. The currents in both the NED and BODY frame are accurately estimated using C2. The third plot of Figure 4 shows the estimated (solid blue and red lines) and actual (dashed yellow and purple lines) currents in the NED frame, while the fourth plot of Figure 4 shows the estimated (blue and red lines) and actual (dashed yellow and purple lines) currents in the BODY frame. From the bottom plot of Figure 4 it is clear that the desired heading is tracked accurately.

C2 also includes estimates of the higher order currents in the NED frame. These are given in Figure 5. Estimated currents are represented by the blue, red and yellow solid lines while the actual currents are given by the dashed purple line. The higher order current estimates are not guaranteed to converge to the actual values and it is clear from Figure 5 that they do not. The control objectives as described in (1) and (2) are, however, still achieved.

VII. Experiment at SINTEF ACE Live Fish Farm

A. Experimental Setup and Vehicle Description

To experimentally validate controller C1, a set of field experiments was conducted in a fish cage at SINTEF ACE, a full-scale aquaculture laboratory off the coast of Norway. The experiments were conducted in the presence of fish, but these were in no way affected by the presence of the ROV. Thus, the experiments did not require review or oversight from a governing body or ethics committee.

The vehicle used in the field trials was a 90 kg Argus Mini ROV with dimensions 0.9m, 0.65m, 0.6m, in length, width and height, respectively.

The ROV has four horizontal thrusters and two vertical thrusters. The horizontal thrusters have azimuth angles of $\alpha = \pm 35^\circ$, actuating the surge, sway and yaw DOFs. A Nortek 1000 Doppler Velocity Logger (DVL) was used to measure the distance, velocity and heading relative to the net structure.

B. Practical Implementation Aspects of Controller C1

The ROV used in the field trials has thrusters that may saturate. Furthermore, the adapted terms generated by (16) may increase to infeasible, unrealistic values due to e.g. measurement noise. As such, two anti-windup schemes are implemented as part of the controller C1.

1) Clamping: Clamping is a rather simple anti-windup scheme that stops the estimated states from growing when the thrusters are saturated, i.e.,

$$\dot{\hat{\boldsymbol{V}}}_c = \begin{cases} \boldsymbol{0}, & \text{if } \tau_{\max,n} < \tau_{\mathrm{DOF},n} < \tau_{\min,n} \\ & \quad \wedge \operatorname{sign}\left(\dot{\hat{\boldsymbol{V}}}_c\right) = \operatorname{sign}\left(\tau_{\mathrm{DOF},n}\right) \\ -\boldsymbol{\Gamma}\boldsymbol{G}^\top(t)\tilde{\boldsymbol{v}}, & \text{otherwise} \end{cases} \tag{70}$$

where $\tau_{\mathrm{DOF},n}$ is the calculated control force in DOF n and $\tau_{\max,n}$ and $\tau_{\min,n}$ is the maximum and minimum available thrust in DOF n, respectively. The implementation of the clamping algorithm requires the calculation of the maximum actuation force that the ROV can exert in each DOF. The calculated control input is compared to this limit. Furthermore, the clamping algorithm checks if the adaptive law is pushing the control input further into wind-up by comparing the signs.

2) Projection: The second anti-windup scheme implemented is projection. The projection operator is designed to keep the estimated variables within a pre-defined bound. In this particular case, the ocean currents in $\{n\}$ are estimated. As such and upper bound $\hat{V}_{\max} \leq V_{\max}$ as stated in Assumption 7 is used in the projection. A projection scheme similar to that given in [47] is used in this work and is defined as follows

$$\dot{\hat{V}}_i = \gamma_i \mathrm{Proj}(\hat{V}_i, y_p) \tag{71}$$

with $y_p = \boldsymbol{G}^\top \tilde{\boldsymbol{v}}$, and

$$\mathrm{Proj}(\hat{V}_i, y_p) \triangleq \begin{cases} y_p, \text{ if } g(\hat{V}_i) < 0 \vee g(\hat{V}_i) \geq 0 \wedge \nabla g^\top y_p \leq 0 \\ y_p - \frac{\nabla g \nabla g^\top y_p g}{\|\nabla g\|^2}, \text{ if } g(\hat{V}_i) \geq 0 \wedge \nabla g^\top y_p \geq 0 \end{cases}. \tag{72}$$

where

$$g(\hat{V}_i) = \frac{(\epsilon_{V_i} + 1)\hat{V}_i^\top \hat{V}_i - V_{\max}^2}{\epsilon_{V_i} V_{\max}^2} \tag{73}$$

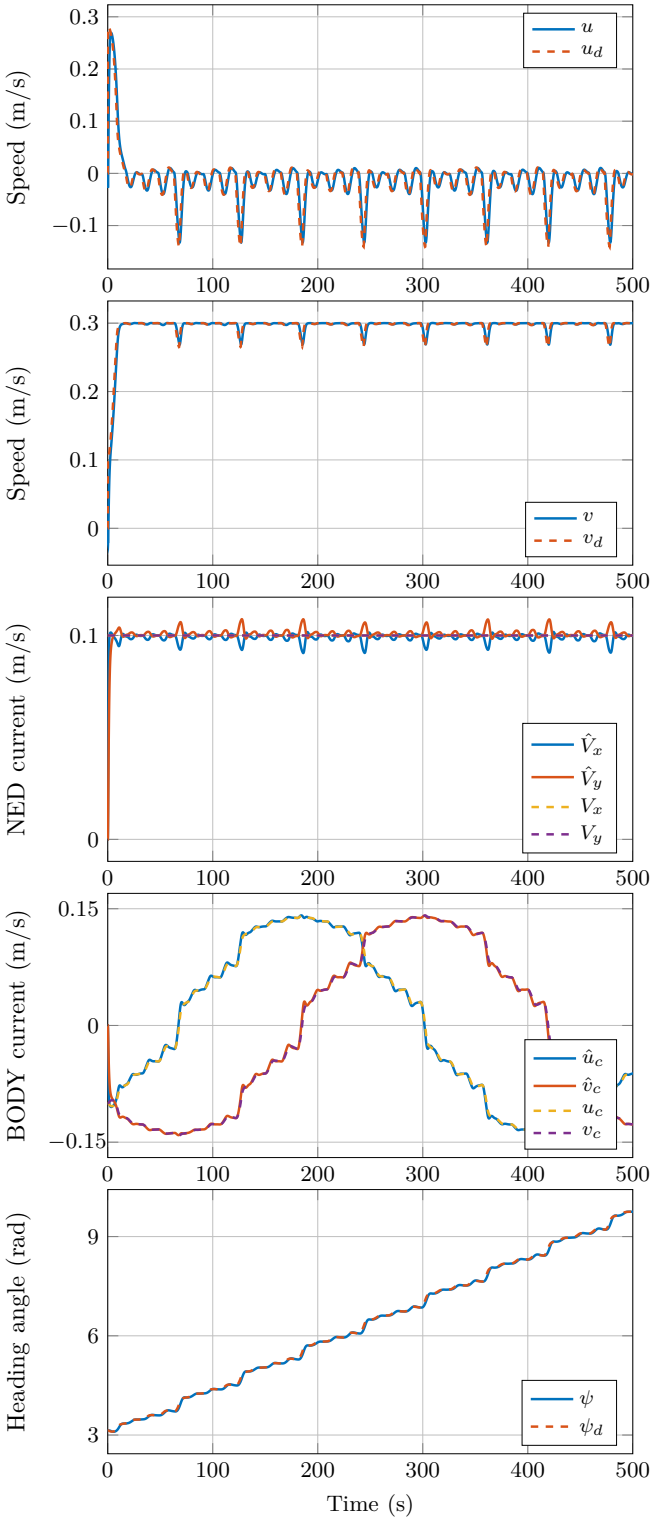

Fig. 3: Results from simulations of C1 and the heading controller on the control plant model.

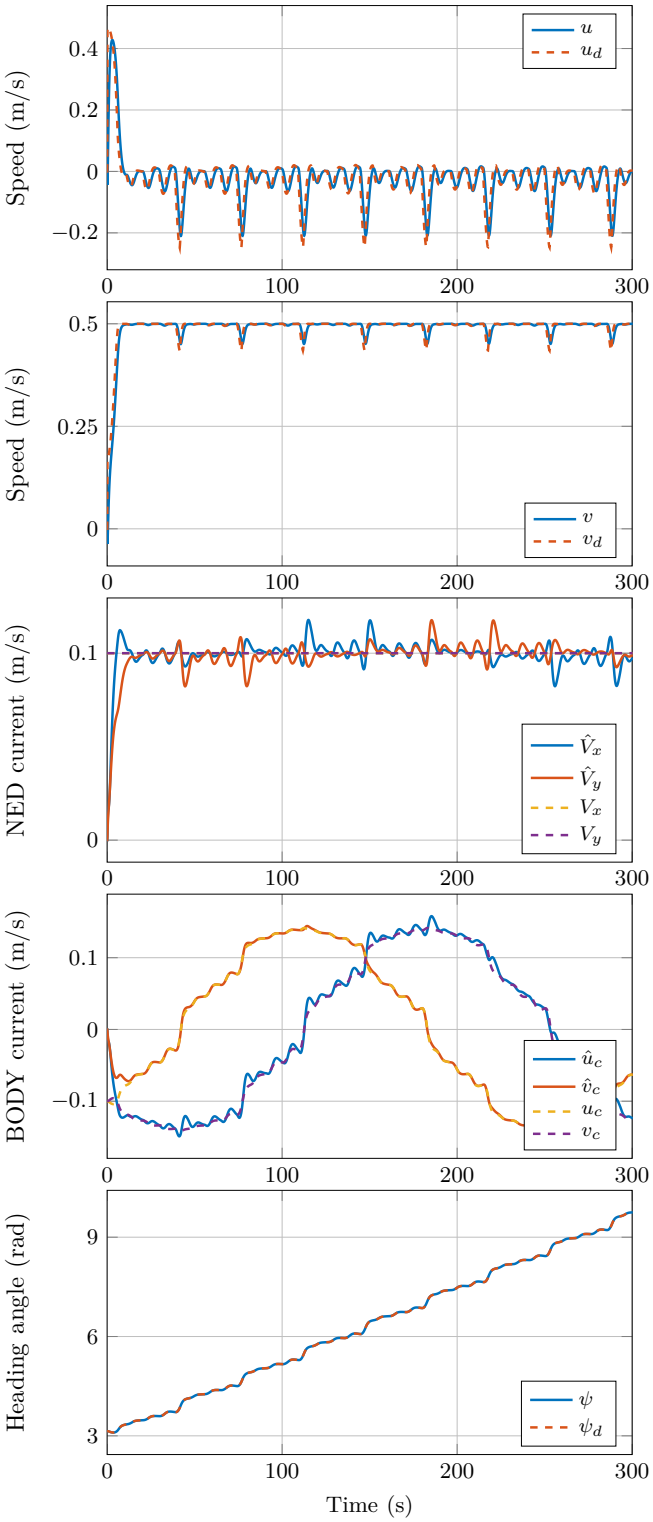

Fig. 4: Results from simulations of C2 on the control plant model.

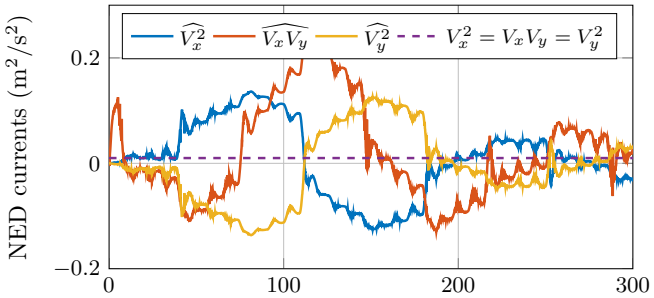

Fig. 5: Estimates of the higher order NED currents from simulations of C2 on the control plant model.

is a smooth function with $\epsilon_{V_i} > 0$ as the projection tolerance bound, $||\hat{V}_i|| \leq V_{\max}^2$ and gradient $\nabla g(\hat{V}_i) = 2\frac{\epsilon_{V_i}+1}{\epsilon_{V_i} V_{\max}^2}\hat{V}_i$.

3) Controller Tuning for Field Trial: Experience from previous sea trials recommends to relax the controller gains obtained from simulations. Therefore, the time constant for the C1 reference model in surge and sway was set to $T = 1.0$s. The projection operator was tuned with $V_{\max} = 0.5$ and projection tolerance $\epsilon_{V_i} = 1.0$. The adaptive laws were tuned with $\gamma_x = \gamma_y = 2.0$ and the proportional gain $k_{p_u} = k_{p_v} = 5.0$.

The heading controller used with C1 in the simulations is a PD controller, as no disturbances are present in the heading degree of freedom. This was not the case for the field trial experiments where it was quickly identified that the heading did not converge to the desired value. As such, and integral term was added to the heading controller. The PID controller parameters were tuned to $k_{p_\psi} = 15$, $k_{i_\psi} = 0.5$ and $k_{d_\psi} = 1.0$. All parameters were found through trial and error.

C. Results From Field Trials

Figure 6 shows the results from using C1 at the SINTEF ACE full scale aquaculture laboratory. The top two plots show the velocities and it is clear that the controller is able to track the reference velocities satisfyingly, with small deviations. At $t \sim 350\text{s} - 370\text{s}$, the thrusters saturate which leads to a small deviation between actual and desired sway velocity. Plots three and four of Figure 6 show the estimated ocean current in NED (third plot) and BODY (fourth plot). The actual ocean current values are unknown, hence it is not possible to verify the estimated values. Looking at the third plot it is clear that when the thrusters saturate between $t \sim 350\text{s} - 370\text{s}$ the projection operator is stopping the estimation of $\hat{V}_x$, but is causing some oscillatory behaviour. The bottom plot of Figure 6 shows the heading which is satisfyingly controlled using a PID controller.

A PI controller was formerly used to control the velocities. Results from a trial in similar operating conditions using this PI controller is shown in Figure 7. It is clear that a deviation is present in the sway velocity while the surge velocity is controlled quite well. Attempts were made to reduce the error in the sway velocity by increasing the integral gain, but this lead to instabilities most probably caused by signal noise. Figure 8 shows the errors between the desired and actual surge and sway speeds for both controller C1 and the PI controller (taken at different, but similar trials). From this

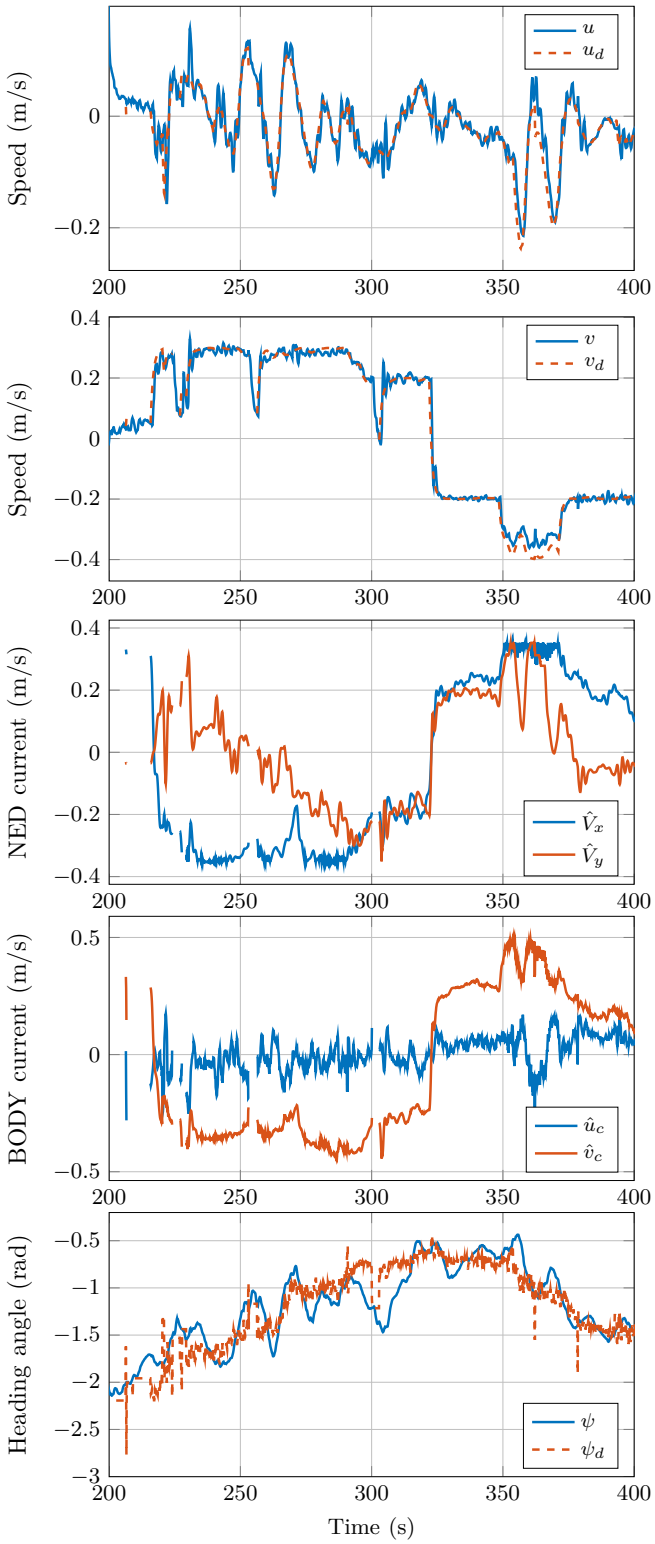

Fig. 6: Results from field trials at SINTEF ACE using controller C1 to control the surge and sway velocities, and a PID controller for the heading angle.

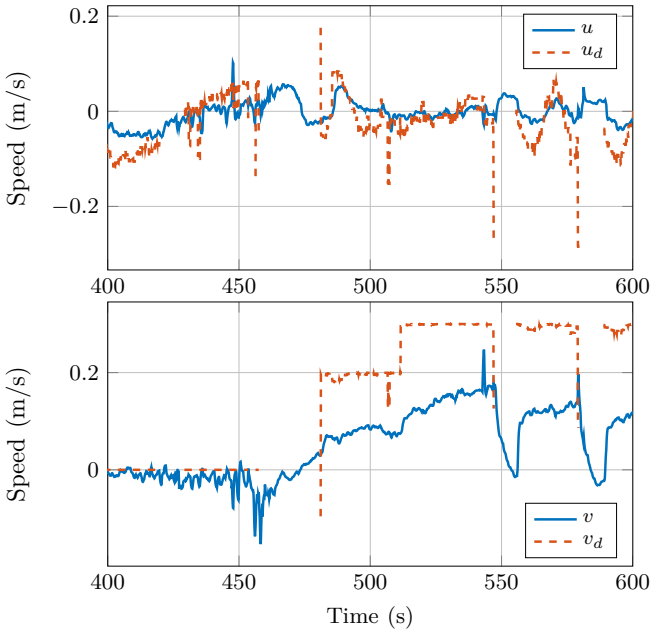

Fig. 7: The surge and sway velocities using a PI controller.

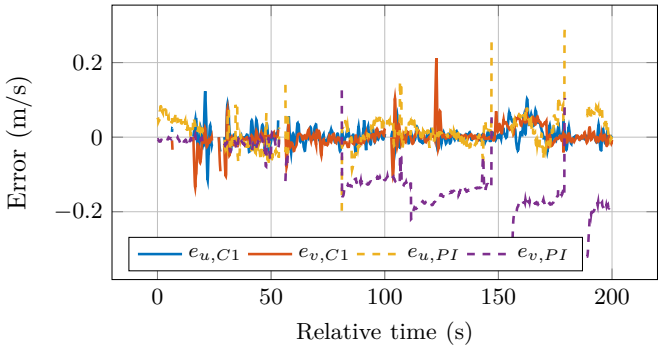

Fig. 8: Comparison of error in surge and sway velocities using a PI controller and the proposed controller C1.

it is clear that the proposed controller C1 has a lower overall error compared to a PI controller (the time axis is adjusted in order to plot the two trials in the same figure. Thus the relative time is shown).

Note that the net following guidance system deactivates (reference speeds are set to zero) if the signal from the DVL is lost. This signal loss is often caused by fish swimming in front of the sensor [48]. Data from these instances (e.g. between $t \sim 200 - t \sim 220$ of Figure 6 and between $t \sim 460 - t \sim 480$ of Figure 7) are not shown in the figures.

VIII. Conclusion and Future Work

This paper has presented two control laws for tracking time-varying reference values in the surge, sway, and yaw DOFs. The controllers are combined with a path-following algorithm to enable autonomous traversal of an aquaculture net pen. The main contributions of this paper are the proposed control laws, with properties that ensure asymptotic convergence of the error states to zero, as well as a validation in a field trial, where one of the controllers was implemented on an industrial ROV and tested in realistic conditions.

For the proposed controller, C1, the origin of the closed-loop system with the adaptive law was proven to be UGAS. Furthermore, clamping and projection were implemented as anti-windup schemes in the field trial to ensure that thruster saturation does not lead to unwanted behaviour. The controller was validated in both simulations and field trials, showing promising results.

For the second proposed controller, C2, the origin of the closed-loop system with the adaptive laws was proven to be UGS and the error variable containing the controlled velocities and the heading angle was proven to converge to zero. This controller augments C1 with heading control and estimation of the higher order disturbance terms arising from the Coriolis-centripetal forces. This controller was validated through simulations and also showed promising results. The controller managed to track the reference values for the velocities, as well as the reference value for heading while providing accurate estimates of the current disturbance. The higher order disturbance terms were not accurately estimated, but the control objective was still achieved. Validating controller C2 in a field trial and evaluating its robustness remains future work.

Appendix

A. Functional Expression

$$\boldsymbol{g}(\boldsymbol{\theta}, t) = \begin{bmatrix} g_{11} & g_{12} \\ g_{21} & g_{22} \end{bmatrix} \tag{74}$$

where

$$g_{11} = -\frac{m_{11}^A}{m_{11}}(V_x \sin(\psi) - V_y \cos(\psi))$$
$$g_{12} = \frac{d_{11}}{m_{11}}(V_x \beta_1 + V_y \beta_2)$$
$$g_{21} = -\frac{m_{22}^A}{m_{22}}(V_x \cos(\psi) + V_y \sin(\psi))$$
$$g_{22} = -\frac{d_{22}}{m_{22}}(V_x \beta_2 - V_y \beta_1)$$

and

$$\beta_1 = \cos(\psi_d(t))\frac{\cos(\tilde{\psi}) - 1}{\tilde{\psi}} - \sin(\psi_d(t))\frac{\sin(\tilde{\psi})}{\tilde{\psi}} \tag{75a}$$
$$\beta_2 = \sin(\psi_d(t))\frac{\cos(\tilde{\psi}) - 1}{\tilde{\psi}} + \cos(\psi_d(t))\frac{\sin(\tilde{\psi})}{\tilde{\psi}}. \tag{75b}$$

Note that the terms $g_{(\cdot)}$ in (74) are function of $\tilde{\psi}$ and t, hence of $\boldsymbol{\theta}$ and t, since $\psi = \tilde{\psi} + \psi_d(t)$, but the arguments are dropped to avoid a cumbersome notation; *idem* for β_1 and β_2.

References

[1] FAO, *The State of World Fisheries and Aquaculture 2022. Towards Blue Transformation*, Rome, FAO, 2022.

[2] The Norwegian Directorate of Fisheries, "Aquaculture statistics," 2021, data retrieved from https://www.fiskeridir.no/Akvakultur/Tall-og-analyse/Akvakulturstatistikk-tidsserier/Laks-regnbueoerret-og-oerret/Matfiskproduksjon.

[3] H. V. Bjelland, M. Føre, P. Lader, D. Kristiansen, I. M. Holmen, A. Fredheim, E. I. Grøtli, D. E. Fathi, F. Oppedal, I. B. Utne, and I. Schjølberg, "Exposed aquaculture in Norway," in *OCEANS 2015 - MTS/IEEE Washington*, 2015, pp. 1–10.

[4] B. Hersoug, "'one country, ten systems' – the use of different licensing systems in Norwegian aquaculture," *Marine Policy*, vol. 137, p. 104902, 2022.

[5] I. B. Utne, I. Schjølberg, and I. M. Holmen, "Reducing risk in aquaculture by implementing autonomous systems and integrated operations," in *Proc. European Safety and Reliability Conference (ESREL)*, 2015.

[6] M. Føre, K. Frank, T. Norton, E. Svendsen, J. A. Alfredsen, T. Dempster, H. Eguiraun, W. Watson, A. Stahl, L. M. Sunde, C. Schellewald, K. R. Skøien, M. O. Alver, and D. Berckmans, "Precision fish farming: A new framework to improve production in aquaculture," *Biosystems Engineering*, vol. 173, pp. 176–193, 2018.

[7] K. H. Ang, G. Chong, and Y. Li, "PID control system analysis, design, and technology," *IEEE Transactions on Control Systems Technology*, vol. 13, 2005.

[8] H. B. Amundsen, W. Caharija, and K. Y. Pettersen, "Autonomous ROV inspections of aquaculture net pens using DVL," *IEEE Journal of Oceanic Engineering*, 2021.

[9] E. Børhaug, A. Pavlov, and K. Y. Pettersen, "Integral LOS control for path following of underactuated marine surface vessels in the presence of constant ocean currents," *Proceedings of the 47th IEEE Conference on Decision and Control*, 2008.

[10] S. Moe, W. Caharija, K. Y. Pettersen, and I. Schjølberg, "Path following of underactuated marine surface vessels in the presence of unknown ocean currents," *Proc. of American Control Conference (ACC)*, 2014.

[11] W. Caharija, K. Y. Pettersen, M. Bibuli, P. Calado, E. Zereik, J. Braga, J. T. Gravdahl, A. J. Sørensen, M. Milovanović, and G. Bruzzone, "Integral line-of-sight guidance and control of underactuated marine vehicles: Theory, simulations and experiments," *IEEE Transactions on Control Systems Technology*, vol. 24, 2016.

[12] T. I. Fossen, A. Loria, and A. Teel, "A theorem for UGAS and ULES of (passive) nonautonomous systems: Robust control of mechanical systems and ships," *International Journal of Robust and Nonlinear Control*, vol. 11, pp. 95–108, 2001.

[13] K. D. Do, J. Pan, and Z.-P. Jiang, "Robust adaptive control of underactuated ships on a linear course with comfort," *Ocean Engineering*, vol. 30, no. 17, pp. 2201–2225, 2003.

[14] K. D. Do and J. Pan, "Global robust adaptive path following of underactuated ships," *Automatica*, vol. 42, no. 10, pp. 1713–1722, 2006.

[15] T. I. Fossen and J. P. Strand, "Tutorial on nonlinear backstepping: Applications to ship control," *Modeling, Identification and Control*, vol. 20, no. 2, pp. 83–134, 1999.

[16] S. Das, A. Bhatt, and S. E. Talole, "UDE based backstepping design for ship autopilot," *International Conference on Industrial Instrumentation and Control*, pp. 417–422, 2015.

[17] Z. Liu and R. Chu, "Robust adaptive heading control for a surface vessel with drift angles," *Ocean Engineering*, vol. 205, p. 107310, 2020.

[18] J. Du, C. Guo, S. Yu, and Y. Zhao, "Adaptive autopilot design of time-varying uncertain ships with completely unknown control coefficient," *IEEE Journal of Oceanic Engineering*, vol. 32, no. 2, pp. 346–352, 2007.

[19] J. Li, Z. Fan, R. Bu, Q. Li, and J. Hu, "Robust adaptive backstepping design for course-keeping control of ship with parameter uncertainty and input saturation," *International Conference of Soft Somputing and Pattern Recognition*, pp. 63–67, 2011.

[20] S. J. Ohrem, H. B. Amundsen, W. Caharija, and C. Holden, "Robust adaptive backstepping DP control of ROVs," *Control Engineering Practice*, vol. 127, p. 105282, 2022.

[21] J.-H. Li, P.-M. Lee, B.-H. Jun, and Y.-K. Lim, "Point-to-point navigation of underactuated ships," *Automatica*, vol. 44, no. 12, pp. 3201–3205, 2008.

[22] G. Zhang, X. Zhang, and Y. Zheng, "Adaptive neural path-following control for underactuated ships in fields of marine practice," *Ocean Engineering*, vol. 104, pp. 558–567, 2015.

[23] Z. Sun, G. Zhang, B. Yi, and W. Zhang, "Practical proportional integral sliding mode control for underactuated surface ships in the fields of marine practice," *Ocean Engineering*, vol. 142, pp. 217–223, 2017.

[24] S.-L. Dai, C. Wang, and F. Luo, "Identification and learning control of ocean surface ship using neural networks," *IEEE Transactions on Industrial Informatics*, vol. 8, no. 4, pp. 801–810, 2012.

[25] H. Khalil, *Nonlinear systems*, 3rd ed. Prentice Hall, 2002.

[26] E. McGookin, D. Murray-Smith, Y. Li, and T. I. Fossen, "Ship steering control system optimisation using genetic algorithms," *Control Engineering Practice*, vol. 8, no. 4, pp. 429–443, 2000.

[27] L. Yuan and H.-S. Wu, "Terminal sliding mode fuzzy control based on multiple sliding surfaces for nonlinear ship autopilot systems," *Journal of Marine Science and Application*, vol. 9, pp. 425–430, 2010.

[28] A. Levant, "Sliding order and sliding accuracy in sliding mode control," *International journal of control*, vol. 58, no. 6, pp. 1247–1263, 1993.

[29] B. O. Haugaløkken, H. B. Amundsen, H. S. Fadum, J. T. Gravdahl, and S. J. Ohrem, "Adaptive generalized super-twisting tracking control of an underwater vehicle," in *2023 IEEE Conference on Control Technology and Applications (CCTA)*. IEEE, 2023, pp. 687–693.

[30] K. H. Nguyen, "Control of unmanned subsea vehicles operating at exposed fish farms in presence of environmental disturbances," Master's thesis, NTNU, 2021.

[31] O. J. Sørdalen and O. Egeland, "Exponential stabilization of nonholonomic chained systems," *IEEE transactions on Automatic Control*, vol. 40, no. 1, pp. 35–49, 1995.

[32] P. A. Ioannou and J. Sun, *Robust adaptive control*. PTR Prentice-Hall Upper Saddle River, NJ, 1996, vol. 1.

[33] D. H. Kim and N. Kim, "An auto weather-vaning system for a DP vessel that uses a nonlinear controller and a disturbance observer," *International Journal of Naval Architecture and Ocean Engineering*, vol. 6, no. 1, pp. 98–118, 2014.

[34] S. Fan and C. A. Woolsey, "Underwater vehicle control and estimation in nonuniform currents," *American Control Conference*, pp. 1400–1405, 2013.

[35] H. Ø. Karlsen, H. B. Amundsen, W. Caharija, and M. Ludvigsen, "Autonomous aquaculture: Implementation of an autonomous mission control system for unmanned underwater vehicle operations," in *OCEANS 2021: San Diego–Porto*. IEEE, 2021, pp. 1–10.

[36] A. J. Sørensen, "Structural issues in the design and operation of marine control systems," *Annual Reviews in Control*, vol. 29, pp. 125–149, 2005.

[37] G. Antonelli, *Underwater Robots: Motion and Force Control of Vehicle-Manipulator Systems*. Springer, 2006.

[38] T. I. Fossen, *Handbook of Marine Craft Hydrodynamics and Motion Control*. John Wiley & Sons Ltd, 2011.

[39] A. E. Taylor, "L'hospital's rule," *The American Mathematical Monthly*, vol. 59, no. 1, pp. 20–24, 1952. [Online]. Available: http://www.jstor.org/stable/2307183

[40] E. Panteley and A. Loría, "On global uniform asymptotic stability of nonlinear time-varying systems in cascade," *Systems & Control Letters*, vol. 33, pp. 131–138, 1998.

[41] A. A. J. Lefeber, *Tracking control of nonlinear mechanical systems*. universiteit Twente Enschede, 2000.

[42] E. Panteley, E. Lefeber, and A. Loría, "Exponential tracking control of a mobile car using a cascaded approach," *IFAC Proceedings Volumes*, vol. 31, pp. 201–206, 1998.

[43] J.-J. E. Slotine, W. Li *et al.*, *Applied nonlinear control*. Prentice hall Englewood Cliffs, NJ, 1991, vol. 199, no. 1.

[44] K.-J. Reite, M. Føre, K. G. Aarsæther, J. Jensen, P. Rundtop, L. T. Kyllingstad, P. C. Endresen, D. Kristiansen, V. Johansen, and A. Fredheim, "FhSim - time domain simulation of marine systems," *Proceedings of the ASME 2014 33rd International Conference on Ocean, Offshore and Arctic Engineering*, 2014.

[45] B. Su, K.-J. Reite, M. Føre, K. G. Aarsæther, M. O. Alver, P. C. Endresen, D. Kristiansen, J. Haugen, W. Caharija, and A. Tsarau, "A multipurpose framework for modelling and simulation of marine aquaculture systems," *Proceedings of the ASME 2019 38th International Conference on Oceanm Offshore and Arctic Engineering*, 2019.

[46] P. C. Endresen, J. Birkevold, M. Føre, A. Fredheim, D. Kristiansen, and P. Lader, "Simulation and validation of a numerical model of a full aquaculture net-cage system," in *International Conference on Offshore Mechanics and Arctic Engineering*, vol. 45493. American Society of Mechanical Engineers, 2014, p. V007T05A006.

[47] S. J. Ohrem, T. T. Kristoffersen, and C. Holden, "Adaptive feedback linearizing control of a gas liquid cylindrical cyclone," *IEEE Conference on Control Technology and Applications (CCTA)*, 2017.

[48] P. Rundtop and K. Frank, "Experimental evaluation of hydroacoustic instruments for ROV navigation along aquaculture net pens," *Aquacultural Engineering*, vol. 74, pp. 143–156, 2016.